

Solvent Entrainment in and Flocculation of Asphaltenic Aggregates Probed by Small-Angle Neutron Scattering

Keith L. Gawrys,[†] George A. Blankenship, and Peter K. Kilpatrick*

Department of Chemical and Biomolecular Engineering, North Carolina State University, Raleigh, North Carolina 27965-7905

Received September 14, 2005. In Final Form: January 30, 2006

While small-angle neutron scattering (SANS) has proven to be very useful for deducing the sizes and masses of asphaltenic aggregates in solution, care must be taken to account for solvation effects within the aggregates so as to not err in the characterization of these important systems. SANS measurements were performed on solutions of asphaltenes dispersed in deuterated solvents in which a broad spectrum of solute and solvent chemical compositions was represented. Fits to the scattering intensity curves were performed using the Guinier approximation, the Ornstein–Zernike (or Zimm) model, a mass-fractal model, and a polydisperse cylinder model. The mass-fractal model provided apparent fractal dimensions (2.2–3) for the aggregates that generally decreased with increasing aggregate size, indicating increased surface roughness for larger aggregates. The polydisperse cylinder model provided typical values of the particle thicknesses from 5 to 32 Å, the average particle radius from 25 to 125 Å, and ~30% radius polydispersity. Subsequent calculation of average aggregate molar masses suggested a range of solvent entrainment from 30 to 50% (v/v) within the aggregates that were consistent with previous viscosity measurements. Additional calculations were performed to estimate the proportion of microparticle to nanoparticle aggregates in the solutions. The results indicate that the inclusion of solvation effects is essential for the accurate determination of aggregate molecular weights and fractal dimensions.

Introduction

Petroleum asphaltenes are well-known for their tendency to associate in solution and adsorb at interfaces, implicating them in petroleum production problems such as organic deposition^{1,2} and water-in-crude oil emulsion formation.^{3–11} Fundamental research has focused on establishing a link between asphaltene chemical composition, molecular structure, and colloidal properties. These efforts are complicated by the fact that asphaltenes, the portion of crude oil insoluble in *n*-heptane (or *n*-pentane),¹² are comprised of a polydisperse mixture of chemically heterogeneous species¹³ that can vary significantly from one crude oil to another. In general, the asphaltene molecular structure is

characterized by the presence of fused ring aromatic moieties, small aliphatic side chains, and polar heteroatom-containing functional groups.^{14–18} The chemical composition of asphaltenes is also polydisperse, with typical atomic H/C ratios varying between 1.0 and 1.3 and N, S, and O contents of a few weight percent.^{19–22} Fourier transform infrared (FTIR) and X-ray absorption near-edge (XANE) spectroscopy reveal several polar functional groups, such as carboxylic acids, carbonyls, phenols, pyrroles, and pyridines, that are capable of participating in proton donor–acceptor interactions.^{23–25}

The aggregation mechanism for asphaltenes is primarily governed by van der Waals dispersion interactions, electrostatic interactions between molecular charges, hydrogen bonding of polar moieties, and orientation-dependent repulsive steric interactions, with lesser contributions stemming from intermolecular charge transfer and weak inductive interactions.²⁶ A recent

* Corresponding author. Phone: (919)-515-7121. E-mail: peterk@eos.ncsu.edu.

[†] Present address: Nalco Company, Sugar Land, TX 77478.

(1) Hammami, A.; Phelps, C. H.; Monger-McClure, T.; Little, T. M. *Energy Fuels* **2000**, *14* (1), 14–18.

(2) Karan, K.; Hammami, A.; Flannery, M.; Stankiewicz, B. A. *Pet. Sci. Technol.* **2003**, *21* (3–4), 629–645.

(3) Taylor, S. D.; Czarniecki, J.; Masliyah, J. *J. Colloid Interface Sci.* **2002**, *252* (1), 149–160.

(4) Yarranton, H. W.; Hussein, H.; Masliyah, J. H. *J. Colloid Interface Sci.* **2000**, *228* (1), 52–63.

(5) Khristov, K.; Taylor, S. D.; Czarniecki, J.; Masliyah, J. *Colloids Surf., A* **2000**, *174* (1–2), 183–196.

(6) Havre, T. E.; Sjoblom, J. *Colloids Surf., A* **2003**, *228* (1–3), 131–142.

(7) Aske, N.; Orr, R.; Sjoblom, J.; Kallevik, H.; Oye, G. *J. Dispersion Sci. Technol.* **2004**, *25* (3), 263–275.

(8) Aulflem, I. H.; Kallevik, H.; Westvik, A.; Sjoblom, J. *J. Pet. Sci. Eng.* **2001**, *31* (1), 1–12.

(9) Aske, N.; Kallevik, H.; Sjoblom, J. *J. Pet. Sci. Eng.* **2002**, *36* (1–2), 1–17.

(10) Spiecker, P. M.; Gawrys, K. L.; Trail, C. B.; Kilpatrick, P. K. *Colloids Surf., A* **2003**, *220* (1–3), 9–27.

(11) Spiecker, P. M.; Kilpatrick, P. K. *Langmuir* **2004**, *20* (10), 4022–4032.

(12) Speight, J. G. *The Chemistry and Technology of Petroleum*; Marcel Dekker: New York, 1999; p 881.

(13) Yang, X. L.; Hamza, H.; Czarniecki, J. *Energy Fuels* **2004**, *18* (3), 770–777.

(14) Strausz, O. P.; Peng, P.; Murgich, J. *Energy Fuels* **2002**, *16* (4), 809–822.

(15) Sheremata, J. M.; Gray, M. R.; Dettman, H. D.; McCaffrey, W. C. *Energy Fuels* **2004**, *18* (5), 1377–1384.

(16) Gray, M. R. *Energy Fuels* **2003**, *17* (6), 1566–1569.

(17) Bergmann, U.; Groenzin, H.; Mullins, O. C.; Glatzel, P.; Fetzer, J.; Cramer, S. P. *Pet. Sci. Technol.* **2004**, *22* (7–8), 863–875.

(18) Groenzin, H.; Mullins, O. C.; Eser, S.; Mathews, J.; Yang, M. G.; Jones, D. *Energy Fuels* **2003**, *17* (2), 498–503.

(19) Boduszynski, M. M. *Energy Fuels* **1988**, *2* (5), 597–613.

(20) Boduszynski, M. M. *Prepr. Pap.—Am. Chem. Soc. Div. Pet. Chem.* **1985**, *30*, 626–640.

(21) Bestougeff, M. A. *Bull. Soc. Chim. Fr.* **1967**, (12), 4773.

(22) Spiecker, P. M.; Gawrys, K. L.; Kilpatrick, P. K. *J. Colloid Interface Sci.* **2003**, *267* (1), 178–193.

(23) Boduszynski, M. M.; McKay, J. F.; Latham, D. R. *Proc. Assoc. Asphalt Paving Technol.* **1980**, *49*, 123–143.

(24) Buenrostro-Gonzalez, E.; Andersen, S. I.; Garcia-Martinez, J. A.; Lira-Galeana, C. *Energy Fuels* **2002**, *16* (3), 732–741.

(25) Mitrakirtley, S.; Mullins, O. C.; Vanelp, J.; George, S. J.; Chen, J.; Cramer, S. P. *J. Am. Chem. Soc.* **1993**, *115* (1), 252–258.

(26) Murgich, J. *Pet. Sci. Technol.* **2002**, *20* (9–10), 983–997.

proposal based on a review of the current literature suggests that strong specific forces, such as interactions between polar heteroatoms or π -bonding between aromatic moieties, drive asphaltene aggregation, while weaker nonspecific dispersion forces dominate asphaltene precipitation.²⁷ Although the intermolecular interactions that drive asphaltene aggregation are generally accepted, debate still exists over the orientation of heteroatom, alkyl, and aromatic moieties within the molecular framework. For example, two different models have been adopted in the literature to account for the degree of aromatic condensation within the fused ring backbone of asphaltenes, but both models are consistent with monomer masses between 500 and 1000 amu. One is the so-called “continental” model of asphaltenes,²⁸ which posits a monomer molecular structure consisting of a large, highly condensed aromatic core surrounded by an aliphatic periphery, as inferred from X-ray diffraction and fluorescence depolarization experiments.^{18,29–33} Interactions of continental monomers would likely form dense-packed aggregates through stacking interactions of the aromatic cores.^{32,33} Alternatively, the so-called “archipelago” model²⁸ was proposed in which individual asphaltene monomers are composed of clusters of polycondensed groups consisting of 5–7 aromatic rings connected by short aliphatic side chains, possibly containing polar heteroatom bridges.^{15,16,32,34,35} The archipelago model is supported by chemical and thermal degradation studies that concluded that the extent of aromatic condensation in asphaltenes is significantly lower than generally believed.³⁵ Furthermore, molecular simulation studies on a proposed Athabasca asphaltene structure suggested that the presence of long aliphatic bridges gives asphaltenes the capacity to fold themselves into a complex three-dimensional globular structure with self-similar internal structure.³² If the archipelago-like structure is valid, it seems probable that asphaltenic aggregates possess a porous, reticulated microstructure susceptible of entraining significant amounts of surrounding solvent.

The notion that asphaltenes entrain solvent or are “swelled” by interactions with the surrounding solvent media is not novel. Swelling of “dry” Cold Lake asphaltenes was evident from the small-angle X-ray scattering (SAXS) spectra as a shift in apparent peak location to lower wavevectors (larger length scales) with increasing dilution by 1-methylnaphthalene.³⁶ Volumetric swelling studies on petroleum asphaltenes showed a solvent-dependent expansion of the packed asphaltene volume (10–70%) with the addition of ~1.5 mL of solvent to 300 mg of dry asphaltenes.³⁷ Other studies suggest that solvation of asphaltenes by the surrounding solvent modifies the aggregate geometry. Viscosity measurements on Khafji asphaltenes in benzene described four alternative means of modeling the hydrodynamic shape of solvated and unsolvated asphaltenic aggregates, depending on assumptions made concerning the thickness of the solvation layer.³⁸ The extent of solvation for Ratawi and Hassi Messaoud asphaltenes in toluene was quantified by measuring the relative viscosity as a function

of solute concentration.^{39,40} Similar calculations of solvent entrainment were obtained from viscosity measurements performed on natural and synthetic Ratawi vacuum residue.⁴¹ The results from these studies suggested that the solvated volume of the asphaltenic aggregates was 1.7–2.7 times the unsolvated or “dry” asphaltene volume, implying a volumetric entrainment of about 40–60%. Similar attempts to quantify the extent of solvation of Safaniya asphaltenes in mixtures of heptane and toluene were performed by a combination of small-angle neutron scattering (SANS) and viscosity measurements;⁴² however, poor agreement of the effective asphaltene volume fraction within the aggregates calculated from the two methods suggested the need to include polydispersity or to modify the assumed aggregate shape.

In this regard, SANS provides the opportunity to quantify the extent of solvent entrainment within asphaltenic aggregates, assuming that the model used to describe the scattering behavior accurately reflects the particle structure. Various monodisperse and polydisperse geometric form factors have previously been applied to SANS and SAXS scattering spectra of asphaltene solutions, including spheres, ellipsoids (prolate or oblate), and cylinders (prolate or oblate).^{43–53} A recent SANS study comparing the quality of fits for various monodisperse and polydisperse structural models suggested that asphaltenic aggregates are described by polydisperse oblate cylinders (or ellipsoids) with a Schultz-like distribution of radii.⁵³ One objective of this study is to show that the polydisperse oblate cylinder model is consistent with the structure of asphaltenic aggregates, regardless of the asphaltene chemical composition solvent conditions. Applying a structural model that accurately describes the asphaltene shape allows additional information to be obtained from scattering data, such as the average aggregate molecular weight. Two methods are provided for calculating the aggregate molecular weight from the SANS fitting parameters. Another objective is to show that self-consistent values of the aggregate molecular weight are obtained from SANS measurements only after properly accounting for solvation effects.

Once the amount of solvent entrainment is known for a given sample, a method is suggested for determining the proportion of microparticle to nanoparticle aggregates in solution. The amount of asphaltene flocculation (or precipitation) is generally measured by gravimetric methods (see, for example, refs 10 and 22). Mason and Lin proposed a method of quantifying the extent of microparticle flocculation from SANS spectra of incompatible crude oil blends using a structure factor based on the Percus–

- (27) Porte, G.; Zhou, H. G.; Lazzari, V. *Langmuir* **2003**, *19* (1), 40–47.
 (28) Murgich, J. *Mol. Simul.* **2003**, *29* (6–7), 451–461.
 (29) Yen, T. F.; Erdman, J. G.; Pollack, S. S. *Anal. Chem.* **1961**, *33* (11), 1587.
 (30) Groenzin, H.; Mullins, O. C. *J. Phys. Chem. A* **1999**, *103* (50), 11237–11245.
 (31) Groenzin, H.; Mullins, O. C. *Energy Fuels* **2000**, *14* (3), 677–684.
 (32) Murgich, J.; Abanero, J. A.; Strausz, O. P. *Energy Fuels* **1999**, *13* (2), 278–286.
 (33) Sharma, A.; Groenzin, H.; Tomita, A.; Mullins, O. C. *Energy Fuels* **2002**, *16* (2), 490–496.
 (34) Calemma, V.; Iwanski, P.; Nali, M.; Scotti, R.; Montanari, L. *Energy Fuels* **1995**, *9* (2), 225–230.
 (35) Strausz, O. P.; Mojelsky, T. W.; Lown, E. M. *Fuel* **1992**, *71* (12), 1355–1363.
 (36) Sirota, E. B. *Pet. Sci. Technol.* **1998**, *16* (3–4), 415–431.
 (37) Carbonegani, L.; Rogel, E. *Energy Fuels* **2002**, *16* (6), 1348–1358.
 (38) Takeshige, W. *J. Colloid Interface Sci.* **2001**, *234* (2), 261–268.

- (39) Sheu, E. Y.; Detar, M. M.; Storm, D. A. *Fuel* **1991**, *70* (10), 1151–1156.
 (40) Bouhadda, Y.; Bendedouch, D.; Sheu, E.; Krallafa, A. *Energy Fuels* **2000**, *14* (4), 845–853.
 (41) Storm, D. A.; Sheu, E. Y. *Fuel* **1993**, *72* (2), 233–237.
 (42) Fenistein, D.; Barre, L.; Broseta, D.; Espinat, D.; Livet, A.; Roux, J. N.; Scarsella, M. *Langmuir* **1998**, *14* (5), 1013–1020.
 (43) Ravey, J. C.; Ducouret, G.; Espinat, D. *Fuel* **1988**, *67* (11), 1560–1567.
 (44) Herzog, P.; Tchoubar, D.; Espinat, D. *Fuel* **1988**, *67* (2), 245–250.
 (45) Sheu, E. Y.; Liang, K. S.; Sinha, S. K.; Overfield, R. E. *J. Colloid Interface Sci.* **1992**, *153* (2), 399–410.
 (46) Espinat, D.; Ravey, J. C.; Guille, V.; Lambard, J.; Zemb, T.; Cotton, J. P. *J. Phys. IV* **1993**, *3*, 181–184.
 (47) Xu, Y. N.; Koga, Y.; Strausz, O. P. *Fuel* **1995**, *74* (7), 960–964.
 (48) Thiyagarajan, P.; Hunt, J. E.; Winans, R. E.; Anderson, K. B.; Miller, J. T. *Energy Fuels* **1995**, *9* (5), 829–833.
 (49) Bardon, C.; Barre, L.; Espinat, D.; Guille, V.; Li, M. H.; Lambard, J.; Ravey, J. C.; Rosenberg, E.; Zemb, T. *Fuel Sci. Technol. Int.* **1996**, *14* (1–2), 203–242.
 (50) Lin, M. Y.; Sirota, E. B.; Gang, H. *Abstr. Am. Chem. Soc.* **1997**, *213*, 66–70.
 (51) Barre, L.; Espinat, D.; Rosenberg, E.; Scarsella, M. *Rev. Inst. Fr. Pet.* **1997**, *52* (2), 161–175.
 (52) Tanaka, R.; Hunt, J. E.; Winans, R. E.; Thiyagarajan, P.; Sato, S.; Takanohashi, T. *Energy Fuels* **2003**, *17* (1), 127–134.
 (53) Gawrys, K. L.; Kilpatrick, P. K. *J. Colloid Interface Sci.* **2005**, *288* (2), 325–334.

Table 1. Ranges of Chemical Compositions (Molar Ratios) for Asphaltene Fractions

H/C	N/C	S/C	O/C
1.09–1.45	0.010–0.025	0.002–0.047	0.012–0.036

Yevick (PY) closure.⁵⁴ The nanoparticle contribution to overall scattering intensity was represented using a geometry-independent model (i.e., the Zimm method); however, the PY closure inherently assumes the asphaltene nanoparticles behave as hard spheres. Both the PY method and the method introduced in this study account for changes in the apparent volume fraction of nanoparticle scatterers after effectively removing the contribution of microscale aggregates from the scattering intensity distribution. In this study, the apparent reduction in the nanoparticle volume fraction is calculated after assuming a fixed value for the solvent entrainment within the aggregates containing a mixture of nanoparticle and microparticle aggregates. Comparison of the nanoparticle volume fraction to the total volume fraction of scatterers provides an estimate of the flocculated material. Flocculation results based on the proposed method will be compared to previous gravimetric solubility measurements for the asphaltenic fractions at the same solvent conditions.

Experimental Section

Asphaltene Precipitation. Asphaltenes were isolated from five crude oils in a 40:1 (v/v) excess of *n*-heptane. The source crude oils included B6, Hondo (HO), Arab Heavy (AH), Gulf Coast (GC), and Canadon Seco (CS). These crude oils were asphaltene rich and varied in viscosity, native resin content, and asphaltene chemical composition. Asphaltenes isolated from the crude oils were separated into more soluble (S) and less soluble (P) fractions by dissolving the whole asphaltenes in toluene and inducing partial precipitation through *n*-heptane addition, according to the procedure of Spiecker et al.¹⁰ A shorthand notation was used to identify the fractions generated by this method. For example, the less soluble fraction of asphaltenes that consisted of 30% (w/w) of the whole asphaltenes was identified as the P30 fraction. The more soluble fraction that consisted of 70% (w/w) of the whole asphaltenes was identified as the S70 fraction.

B6 and HO asphaltenes were also separated into several fine fractions by sequential fractionation in mixtures of heptane and toluene, according to the procedure of Gawrys et al.⁵⁵ During the fine fractionations, approximately 20 g of whole asphaltenes were dissolved in toluene solution such that the total asphaltene concentration was 1% (w/w) after flocculant addition. Enough heptane was added to the solution to induce partial precipitation of approximately 1–2% (w/w) of the whole asphaltenes. The precipitated asphaltenes were isolated by filtration, becoming the first “fine fraction”. The soluble asphaltenes were recovered from the filtrate and dispersed in a mixture of toluene and heptane according to the above procedure such that another 1–2% (w/w) of the whole asphaltenes precipitated. The fractionation procedure continued using progressively more *n*-heptane as a flocculant until 20–30 fine fractions were generated.

Chemical Characterization. All of the asphaltene fractions were characterized by combustion elemental analysis at the University of Alberta (Department of Chemistry, Edmonton, Alberta, Canada) using a Carlo Erba instrument. A detailed summary of the chemical composition of the asphaltene fractions is described elsewhere.^{22,55} The ranges of chemical compositions for the asphaltene fractions analyzed in this study are shown in Table 1.

SANS Sample Preparation. Solutions with mass concentrations of 1% (w/w) were prepared by dissolving the various asphaltene fractions in mixtures of deuterated solvents, including *d*-toluene, *d*-heptane, *d*-methylnaphthalene, and *d*-methanol. Several combina-

tions of the above solvents were used (e.g., pure *d*-toluene; 40:60 (v/v) *d*-heptane/*d*-toluene; 90:10 (v/v) *d*-methylnaphthalene/*d*-methanol) for the fractions to represent a broad range of asphaltene solubility behaviors. Solvents were obtained from CDN Isotopes and had >99.9% chemical purity and >99.5% perdeuteration. During the sample preparation, *d*-toluene or *d*-methylnaphthalene was initially added to the dry asphaltenes, and the solution was subjected to constant, gentle shaking until the asphaltenes were completely dissolved. Upon dissolution of the asphaltenes, the second solvent (i.e., *d*-methanol or *d*-heptane) was added to the solutions. The solutions were allowed to equilibrate for at least 1 week prior to performing the scattering experiments.

SANS Measurements. SANS measurements were performed on the small-angle neutron diffractometer (SAND) at the Intense Pulsed Neutron Source (IPNS) Division of Argonne National Laboratory (Argonne, IL). The instrument geometry and neutron wavelength values bound the operating Q range according to

$$Q = \frac{4\pi}{\lambda} \sin \theta \quad (1)$$

where θ is half the scattering angle, and λ is the neutron wavelength. The available Q range extended from 0.0035 to 2 \AA^{-1} and was adequate for the modeling of asphaltene aggregation. The samples were measured at 25 °C in cylindrical quartz sample cells (NGS Precision) with a path length of 2 mm. A typical scattering experiment consisted of 15 min of detecting neutron transmission through the samples followed by 60 min of scattering. The absolute scattering intensity, $I(Q)$, for each sample was obtained from the total detector counts corrected for background radiation, the neutron transmission through the sample, the scattering from the quartz cell, and detector sensitivity.

SANS Model Fitting. Scattering intensity versus scattering angle ($I(Q)$ vs Q) curves were fit to the Guinier approximation,⁵⁶ the Ornstein–Zernike (or Zimm) model,⁵⁷ the small-particle mass-fractal model,⁵⁸ and a polydisperse radius oblate cylinder model.⁵³ Both the Guinier and Ornstein–Zernike models provide a means of estimating aggregate sizes without specifying the particle geometry. The Guinier approximation is given by⁵⁶

$$I(Q) = I_0 \exp(-Q^2 R_G^2/3) \quad (2)$$

where I_0 is the scattering intensity extrapolated to $Q = 0$, and R_G is the aggregate radius of gyration. The Guinier approximation is generally applied by fitting a straight line through a plot of $\ln(I)$ versus Q^2 in the range of $Q_{\max} R_G \leq 1$. The Ornstein–Zernike model describes the scattering intensity in the low Q limit as a Lorentzian line shape given by⁵⁷

$$I(Q) = \frac{I_0}{1 + Q^2 R_G^2/3} \quad (3)$$

Several previous studies have applied the Ornstein–Zernike model to asphaltene solutions.^{10,22,42,54,59–61} In many of these studies, the scattering data is generally truncated at an arbitrary value of Q_{\max} . In this study, the Ornstein–Zernike model was applied after truncating the data sets at two different values of Q_{\max} (i.e., $Q_{\max} R_G \leq 1$ and $Q_{\max} = 0.1 \text{\AA}^{-1}$).

The fitting function for the small-particle mass-fractal model was authored by Littrell and provided by Argonne National Laboratory for use with IgorPro software. The fitting function for polydisperse radius oblate cylinders was written by the authors.⁵³ The Q range

(56) Guinier, A.; Fournet, G. *Small Angle Scattering of X-rays*; John Wiley & Sons: New York, 1955.

(57) Zimm, B. H. *J. Chem. Phys.* **1948**, *16* (12), 1093–1099.

(58) Hu, X. J.; Littrel, K.; Ji, S.; Pickles, D. G.; Risen, W. M. *J. Non-Cryst. Solids* **2001**, *288* (1–3), 184–190.

(59) Fenistein, D.; Barre, L. *Fuel* **2001**, *80* (2), 283–287.

(60) Roux, J. N.; Broseta, D.; Deme, B. *Langmuir* **2001**, *17* (16), 5085–5092.

(61) Savvidis, T. G.; Fenistein, D.; Barre, L.; Behar, E. *AIChE J.* **2001**, *47* (1), 206–211.

(54) Mason, T. G.; Lin, M. Y. *Phys. Rev. E* **2003**, *67* (5), 050401(R).

(55) Gawrys, K. L.; Spiecker, P. M.; Kilpatrick, P. K. *Energy Fuels*, in press.

over which both models were applied was fixed between 0.006 and 0.5 \AA^{-1} . A constant background term was included in the model fits to account for incoherent scattering from all nuclei with nonzero spin in the solvent and solute. The small-particle mass-fractal model is given by⁵⁸

$$I(Q) = I_0 \frac{\sin[(D-1) \tan^{-1}(Q\xi)]}{(D-1)Q\xi(1+Q^2\xi^2)^{(D-1)/2}} \quad (4)$$

where D and ξ are the fractal dimension and the exponential cutoff length for fractal aggregation, respectively. Equation 4 is a simplification of the mass-fractal model introduced by Chen and Teixeira⁶² that describes the aggregates as a three-dimensional agglomeration consisting of elementary spherical particles with radius, R , and having a fractal-like nature. The small-particle mass-fractal assumes that scattering from the elementary spherical particles is negligible (i.e., $\xi \gg R$ and $Q_{\max}R \ll 1$). The radius of gyration was determined from the above fitting parameters by

$$R_G^2 = D(D+1)\xi^2/2 \quad (5)$$

In the limit that $D=2$, the small-particle mass-fractal model reduces to the Zimm approximation.

The scattering intensity distribution for a polydisperse system is proportional to the ensemble average of the intraparticle structure factor, $P(Q)$, as given by

$$I(Q) = \int_0^\infty I_0 P(Q,x) f(x) dx \quad (6)$$

where $f(x)$ is a normalized distribution function for size parameter, x . The intraparticle structure factor used in this study to model polydisperse oblate cylinders is given by

$$\langle P(Q) \rangle = \frac{\int_0^\infty V^2 P_{\text{ob},1}(Q,R) f_S(R) dR}{\int_0^\infty V^2 f(R) dR} \quad \{QR < 3\}$$

$$\langle P(Q) \rangle = \frac{\int_0^\infty V^2 P_{\text{ob},2}(Q,R) f_S(R) dR}{\int_0^\infty V^2 f(R) dR} \quad \{QR > 3\} \quad (7)$$

where f_S is the Schultz distribution function. The polydisperse cylinder model utilizes two approximations of the intraparticle structure factor for an oblate cylinder. In the low Q region (i.e., $QR < 3$), the intraparticle structure factor for a monodisperse oblate cylinder of radius R and thickness L may be written as⁶³

$$P_{\text{ob},1}(Q) = 2 \left[\frac{\sin(QL/2)}{QL/2} \right]^2 \left[\frac{1 - J_1(2QR)/QR}{(QR)^2} \right] \quad (8)$$

where $J_1(x)$ is the first-order Bessel function of the first kind. In the high Q region (i.e., $QR > 3$), the intraparticle structure factor was described by an exponential approximation given by⁵⁶

$$P_{\text{ob},2}(Q) = \frac{2}{(QR)^2} \exp\left(-\frac{(QL)^2}{12}\right) \quad (9)$$

Additional details of the model development are located elsewhere.⁵³ The average radius of gyration for polydisperse cylinders with a Schultz distribution of radii is given by⁵⁰

$$\langle R_G \rangle^2 = \frac{L^2}{3} + \frac{\langle R^6 \rangle}{2\langle R^4 \rangle} \quad (10)$$

where R_{avg} is the mean particle radius, and z is the Schultz

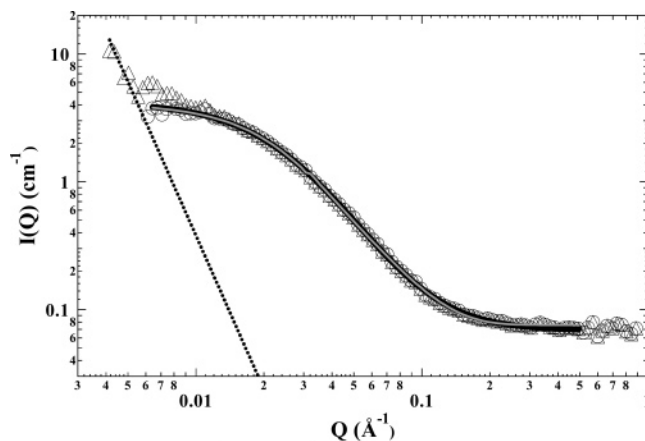


Figure 1. Example model fits to scattering curve for HO asphaltenes (1 wt %) in 40:60 *d*-heptane/*d*-toluene (v/v). Legend: (triangles) raw data; (dashed line) power-law fit; (circles) power-law-corrected data; (black line) mass-fractal fit; (gray line) polydisperse cylinder fit.

polydispersity parameter. The Schultz polydispersity parameter is related to the standard deviation in the radius (σ_R) by

$$z = \left(\frac{R_{\text{avg}}}{\sigma_R} \right)^2 - 1 \quad (11)$$

Results and Discussion

Model Fit Parameters. The scattering intensity versus scattering angle ($I(Q)$ vs Q) curve for a 1% (w/w) solution of HO asphaltenes in 40:60 *d*-heptane/*d*-toluene (v/v) is shown in Figure 1. The sharp rise in the scattering intensity at low Q values for the raw data (triangles) indicated the presence of asphaltenic flocs of roughly micron-sized dispersed in solution.^{22,54,60} Since the Porod-like upturns did not exhibit a plateau at the lowest scattering angles, it was not possible to determine the size of the flocs from these scattering experiments. Therefore, the contribution of these agglomerates to the scattering intensity distributions were effectively removed by fitting a power-law function with an exponent of -4 (i.e., $I(Q) \sim Q^{-4}$) through the three lowest Q data points for this solution, extrapolating the power-law function to higher Q values, and subtracting it from the original scattering data over the entire available Q range. The corresponding power-law fit appears as the dashed line in Figure 1. As seen in the figure, the resulting power-law-subtracted scattering curve (\circ) reveals the scattering behavior from nanoscale aggregates in this solution. The above power-law correction was only applied to the scattering intensity curves in which the Guinier plateau did not extend to $Q = 0.006 \text{ \AA}^{-1}$.

Nonlinear least-squares fits of the small-particle mass-fractal (black line) and polydisperse radius, oblate cylinder (gray line) models to the scattering intensity curve are also shown in Figure 1. Parameters obtained from the various model fits to HO asphaltenes in 40:60 *d*-heptane/*d*-toluene are summarized in Table 2. As shown in the table, the I_0 parameters obtained from both fits to the Ornstein–Zernike model significantly overpredicted the Guinier I_0 parameter, while the mass-fractal and polydisperse cylinder models underpredicted the Guinier I_0 parameter by approximately 7%. The Ornstein–Zernike and mass-fractal models also overpredicted the radii of gyration obtained from the Guinier analysis; however, the value of R_G obtained from the polydisperse cylinder fit agreed with the Guinier R_G parameter within statistical uncertainty.

A more detailed comparison of I_0 and R_G parameters obtained from various model fits to 108 scattering intensity curves is

(62) Chen, S. H.; Teixeira, J. *Phys. Rev. Lett.* **1986**, 57 (20), 2583–2586.

(63) Pedersen, J. S. *J. Appl. Crystallogr.* **2000**, 33 (1), 637–640.

Table 2. Model Fitting Parameters for HO Asphaltenes in 40:60 *d*-Heptane/*d*-Toluene (v/v)

model	I_0 (cm ⁻¹)	R_G (Å)	D	ξ (Å)	χ^2	R_{avg} (Å)	σ_R (Å)	L (Å)
Guinier	4.4 ± 0.1	73 ± 1						
Zimm ($Q_{\text{max}}R_G \sim 1$)	5.2 ± 0.6	100 ± 20						
Zimm ($Q_{\text{max}} = 0.1 \text{ \AA}^{-1}$)	5.6 ± 0.1	109 ± 1						
mass-fractal	4.11 ± 0.05	81 ± 2	2.53 ± 0.02	38.4 ± 0.5	1.4585			
polydisperse cylinder	4.14 ± 0.04	73 ± 2			5.7508	69.4 ± 0.7	22.3 ± 0.1	20.5 ± 0.3

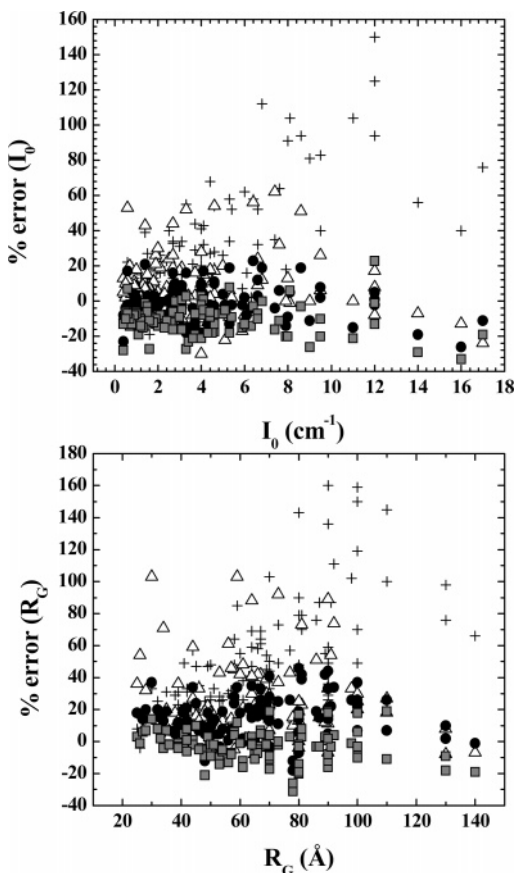


Figure 2. Percent deviation in I_0 and R_G parameters obtained from various model fits to those obtained from Guinier analyses. The abscissae represent the Guinier parameters. Legend: (cross symbols) Ornstein–Zernike model truncated at $Q_{\text{max}} = 0.1 \text{ \AA}^{-1}$; (open triangles) Ornstein–Zernike model truncated at $Q_{\text{max}}R_G \sim 1$; (black circles) small-particle mass-fractal model; (gray squares) polydisperse oblate cylinder model.

shown in Figure 2. In the top and bottom panels, the abscissae represent the values of the Guinier I_0 and R_G parameters, respectively. The ordinate axes represent the percent deviation (% error) in the model fit parameters from the Guinier values. This figure indicates that the Ornstein–Zernike model systematically overpredicted the Guinier parameters, often by greater than 30% and regardless of the selection of Q_{max} . Table 3 presents the average deviation or average percent error in the I_0 and R_G parameters with respect to the Guinier values. It is apparent from Figure 2 and Table 3 that the values of R_G obtained from the small-particle mass-fractal model systematically overpredicted the Guinier R_G values by an average of 15%; however, good agreement was obtained for the values of I_0 . Similarly, the I_0 values obtained from the polydisperse cylinder model underpredicted the Guinier I_0 values by an average of 11%, but good agreement was obtained between the R_G values. These analyses indicate that the values of I_0 and R_G obtained from nonlinear least-squares fits to the scattering data are model-dependent. None of the models employed agreed completely with the Guinier approximation in terms of both the I_0 and R_G parameters.

Table 3. Average Deviation (% error) of I_0 and R_G Parameters with Respect to Guinier Analyses

fitting method	average % error	
	I_0	R_G
Ornstein–Zernike ($Q_{\text{max}} = 0.1 \text{ \AA}^{-1}$)	29	48
Ornstein–Zernike ($Q_{\text{max}}R_G \sim 1$)	10	26
small-particle mass-fractal	-1	15
Polydisperse Oblate Cylinder	-11	-3

In relating the model fitting parameter to the asphaltene aggregation mechanism, it is relevant to discuss the geometry-independent models (i.e., the Ornstein–Zernike and mass-fractal models) with respect to fractal dimension analyses. The mass-fractal model generally provided higher fit qualities to the scattering data over a wider Q range than did the Ornstein–Zernike model. In addition, significant disparities were observed between the I_0 and R_G parameters obtained from the two models. The observation that neither model consistently predicts the Guinier R_G parameter with less than 15% uncertainty suggests that the molecular structure of asphaltenic aggregates is not consistent with a mass-fractal geometry.

A major assumption of the mass-fractal model is that aggregates consist of elementary spherical particles.⁶² For example, Rassamdana and Sahimi⁶⁴ estimated that the mass-to-particle size scaling relationship for diffusion-limited cluster–cluster aggregates with a nanoparticle fractal dimension of 2.5 is consistent with a primary particle size of $\sim 5.8 \text{ \AA}$. This prediction is supported by SAXS⁴⁴ and gel permeation chromatography⁶⁵ data that modeled the molecular structure of asphaltenes as a thin disk with an approximate thickness of 4 Å. X-ray diffraction experiments on Ratawi and Kuwaiti asphaltenes⁶⁶ suggested an average layer diameter of aromatic sheets between 7 and 10 Å and an average distance between aromatic sheets between 3.5 and 3.7 Å. Considering these observations, the elementary particles constituting an asphaltene mass-fractal aggregate might consist of stacks of one to two aromatic sheets, possibly connected to similar aromatic moieties by short, aliphatic linkages. With this in mind, one should be cautious in drawing conclusions concerning the fractal nature of asphaltenic aggregates based on the calculation of an apparent fractal dimension. Figure 3 correlates the apparent fractal dimension (D) with aggregate size parameters (R_G) obtained from the small-particle mass-fractal model for all of the samples analyzed. Open squares represent fractions dissolved in mixtures of *d*-heptane and *d*-toluene, while filled circles represent fractions dissolved in mixtures of *d*-toluene (or *d*-methylnaphthalene) and *d*-methanol. The apparent fractal dimension values for the samples dissolved in mixtures of *d*-heptane and *d*-toluene appeared to decrease with increasing R_G . One possible explanation for this trend is that smaller aggregates are more globular with little surface roughness (i.e., consistent with $D \sim 3$). The amount of surface roughness increases with increasing aggregate size, corresponding to a decrease in the apparent fractal dimension. The samples dissolved in mixtures

(64) Rassamdana, H.; Sahimi, M. *AIChE J.* **1996**, *42* (12), 3318–3332.(65) Acevedo, S.; Escobar, G.; Ranaudo, M. A.; Gutierrez, L. B. *Fuel* **1994**, *73* (11), 1807–1809.(66) Siddiqui, M. N.; Ali, M. F.; Shirokoff, J. *Fuel* **2002**, *81* (1), 51–58.

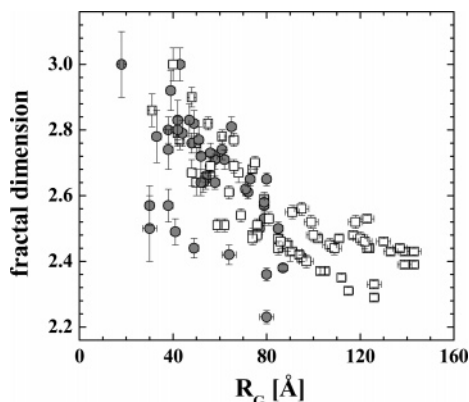


Figure 3. Apparent fractal dimension values from small-particle mass-fractal fits to asphaltene fractions dispersed in (open squares) mixtures of *d*-toluene and *d*-heptane and (filled circles) mixtures of *d*-methyl naphthalene (or *d*-toluene) and *d*-methanol.

containing *d*-methanol appeared to follow a similar trend; however, there was increased dispersion in the data at these solvent conditions. The major implication of Figure 3 that stands in contrast to several previous determinations of the fractal dimension of asphaltene aggregates is that the apparent fractal dimension is not a “fixed” quantity. The fractal dimension varies (i.e., from 2.2 to 3) with asphaltene chemical composition and solvent conditions in a manner that generally trends with the aggregate size.

Several previous studies cite apparently “fixed” values of aggregate fractal dimension for asphaltene aggregates in *d*-toluene that appear to be independent of solute composition, concentration, and/or solvent conditions; however, the range of reported values varies from 1.9 to 3, depending on the analysis method.^{42,45,59,60,64,67} The method of analysis most similar to that shown in Figure 3 involved a polydisperse mass-fractal model in which D was a fitted parameter.⁶⁷ The observed fractal dimension of Ratawi asphaltenes in *d*-toluene ($D \sim 3$) was independent of solute concentration at <40% w/w and consistent with the smallest aggregate formers observed in this study. However, an increase in the number of clusters at higher concentrations (i.e., 40–60% w/w) corresponded to a decrease in the fractal dimension to $D \sim 2$. These results qualitatively agreed with the trend in fractal dimension with aggregate size observed in Figure 3. Since the polydisperse mass-fractal model was only applied to a single asphaltene at a single solvent condition, it is not possible to generalize the result that all asphaltenes at low concentration have a fractal dimension of $D \sim 3$.

Other studies have estimated the apparent fractal dimension from the exponent of scaling relationship between the scattering intensity and the wavevector Q . This method can be problematic in the estimation of apparent fractal dimensions for asphaltenes. For example, the $I(Q) \sim Q^{-D}$ scattering relationship breaks down for small values of Q in which the scattering intensity transitions to the so-called Guinier regime and for large values of Q where the scattering intensity is sensitive either to individual scatterers or to the aggregate surface (i.e., Porod regime).⁶⁸ Therefore, the Q range that describes the “fractal regime” is not easily defined, and the common procedure of extracting the slope from a log–log plot of $I(Q)$ versus Q invariably leads to a value of D that is inconsistent with the one obtained from a fit to a mass-fractal structure factor.⁶²

The value of the apparent fractal dimension may also be obtained from the scaling relationship between the aggregate

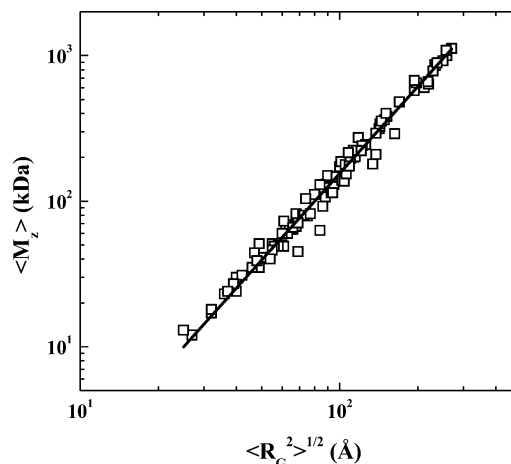


Figure 4. Determination of apparent fractal dimension from the aggregate molecular weight versus aggregate size scaling relationship based on Ornstein–Zernike model fitting parameters.

molecular weight and aggregate size (i.e., $M \sim R_G^D$). For example, Figure 4 shows the mass-size scaling relationship based on parameters from the Ornstein–Zernike model for the 108 samples in this study. The slope of the solid line in the figure represents the apparent fractal dimension given by $D = 1.98$. This value was consistent with other studies that used the Ornstein–Zernike model to fit asphaltene scattering data.^{42,60,65} Each of the previous studies reported apparent fractal dimension values of $D \sim 2$ that were independent of the parameters that typically influence aggregate size (e.g., solvent conditions, temperature, concentration, and fractionation). The apparent trend in fractal dimension with aggregate size (Figure 3) suggests that it is inappropriate to assume that all asphaltenic aggregates will have the same fractal dimension. Furthermore, with no objective measure of the quality of fit, such as reduced χ^2 , it is not possible to judge the reliability of fractal dimensions from either of the above scaling relationships. Mass-fractal structure factor models that incorporate the fractal dimension as a fitted parameter, such as those discussed in this study and in ref 67, provide the least biased means to determine accurate estimates of the aggregate apparent fractal dimension; however, the observed fractal dimension values likely describe the roughness of the aggregate surfaces rather than the internal structure of the asphaltenic aggregates.

As previously described, additional information may be extracted from the scattering behavior of asphaltenic aggregates using a geometry-dependent form factor model, such as the polydisperse radius, oblate cylinder model. As shown in Table 3, the polydisperse cylinder model underpredicted the value of I_0 obtained from Guinier analyses by an average of 11%; however, good agreement was obtained between the aggregate size parameters. The quality of polydisperse cylinder fits to the scattering data, represented by a reduced χ^2 parameter, appeared to decrease with increasing aggregate size, as shown in Figure 5. One possible reason for the decrease in fit quality with increasing aggregate size is the increased contribution of microparticle aggregates to the absolute scattering intensity in the low Q range. As previously described, the apparent microparticle contribution to the scattering curves was removed by fitting a power-law function, $I(Q) \sim Q^{-4}$, through the lowest Q portion of the scattering curves. The selection of an exponent of -4 is somewhat arbitrary, as it assumes that the size of the microparticle aggregates is sufficiently large so that the only contribution to the scattering curve is from Porod scattering; however, it is reasonable to assume that the value of the scaling

(67) Liu, Y. C.; Sheu, E. Y.; Chen, S. H.; Storm, D. A. *Fuel* **1995**, *74* (9), 1352–1356.

(68) Teixeira, J. *J. Appl. Crystallogr.* **1988**, *21*, 781–785.

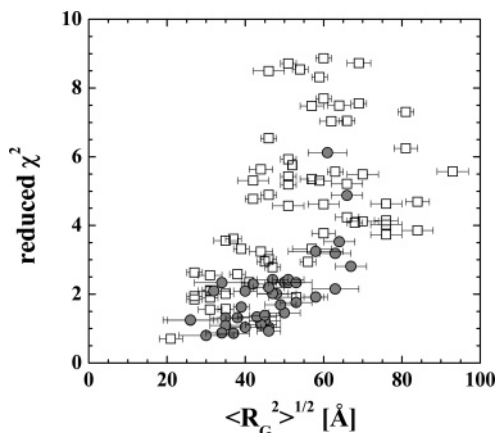


Figure 5. Quality of fit parameters obtained from the polydisperse oblate cylinder model for asphaltene fractions dispersed in (open squares) mixtures of *d*-toluene and *d*-heptane and (filled circles) mixtures of *d*-methyl naphthalene (or *d*-toluene) and *d*-methanol.

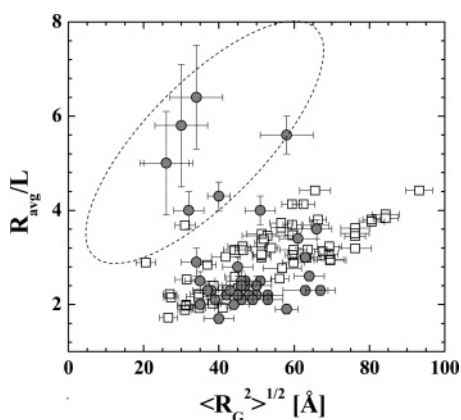


Figure 6. Correlation of particle aspect ratio with average aggregate size parameters obtained from the polydisperse cylinder model for asphaltene fractions in (open squares) mixtures of *d*-heptane and *d*-toluene and (filled circles) mixtures of *d*-methyl naphthalene (or *d*-toluene) and *d*-methanol. Data points inside the dashed oval represent samples with a particle thickness less than 12 Å.

exponent varies from -3 to -4 , depending on the sample composition. Although the observations from Table 3 and Figure 5 suggest that asphaltene aggregates are not perfectly described by the polydisperse oblate cylinder shape, the form factor model employed here provided agreement to the Guinier parameters with respect to other previously applied geometric scattering models.⁵³ Therefore, the polydisperse oblate cylinder model was used in this study to calculate additional parameters from the scattering data, such as the aggregate molecular weight and percentage of entrained solvent.

Figure 6 shows the aspect ratio (R_{avg}/L) obtained from fits of the polydisperse cylinder model for the samples. Data points inside the dashed oval represent aggregates with a particle thickness of less than 12 Å. Neglecting these points, the aspect ratio generally appeared to increase with increasing $\langle R_G^2 \rangle$. Typical particle thicknesses from the model fits ranged from 5 to 32 Å with an average value of 21 ± 6 Å. Typical values of the average particle radius ranged from 25 to 125 Å. If one assumes that an asphaltene monomer consists of groups of condensed aromatic rings containing polar moieties that are interconnected by aliphatic chains, then each aromatic ring system in a given monomer has the potential to interact with aromatic rings from other molecules through dispersion and π -bonding interactions. The aggregation mechanism might then proceed through a series of stacking interactions that expands the aggregate

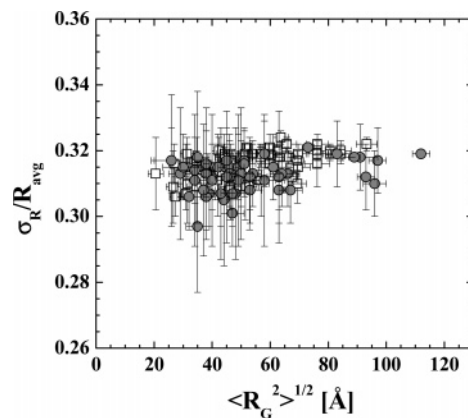


Figure 7. Correlation of radius polydispersity with aggregate size parameters obtained from the polydisperse cylinder model for asphaltene fractions dissolved in (squares) mixtures of *d*-heptane and *d*-toluene and (gray circles) mixtures of *d*-methyl naphthalene (or *d*-toluene) and *d*-methanol.

dimension in the radial direction. As the aggregates grow in radius, more opportunities are created for growth in thickness due to the multiple connected nature of each asphaltene monomer.

The largest outliers from the apparent trend in aspect ratio with $\langle R_G^2 \rangle$ had particle thicknesses less than 12 Å. The presence of *d*-methyl naphthalene in many of these solutions likely disrupted the π -bonding interactions between aromatic sheets. The resulting aggregates tended to have higher aspect ratios (R_{avg}/L), as the aggregation was driven by edge-to-edge interactions of polar moieties, likely through H-bonding, rather than face-to-face interactions of aromatic groups. Figure 7 indicates that the polydispersity (σ_R/R_{avg}) in the aggregate radii is relatively independent of the particle size, with typical values ranging from 30 to 32%. This narrow range of polydispersity values for the samples suggests a similar shape to the aggregate size distributions for asphaltene solutions that is relatively independent of asphaltene chemical composition and solvent conditions.

Solvent Entrainment. Additional information concerning the morphology and composition of asphaltenic aggregates, including the extent of solvent entrainment, was obtained through the calculation of apparent aggregate molecular weight values. The zero- Q scattering intensity is related to the first and second moments of the particle volume (V) as given by

$$I_0 = \frac{\phi \langle V^2 \rangle (\Delta\rho)^2}{\langle V \rangle} \quad (12)$$

where ϕ and $\Delta\rho$ are the volume fraction of scatterers and the difference between the scattering length density of the solvent and scatterers, respectively. The scattering length density difference ($\Delta\rho$) reflects the differing abilities of the solvent and the aggregate to scatter neutrons. For a given phase, j , the scattering length density is a product of the mass density, d_j , and the summation of contributions from individual atomic species, i , as given by

$$\rho_j = d_j \sum_i \frac{b_i x_i}{m_i} \quad (13)$$

where b_i , x_i , and m_i are the bound coherent scattering length, mass fraction, and atomic mass of species i , respectively. In calculating the scattering length density of the solvent, the solvent mass density and chemical composition values are used in eq 13. The calculation of the scattering length density for the aggregates

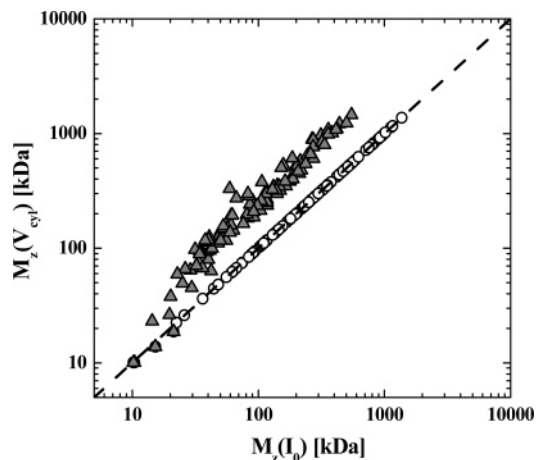


Figure 8. Parity plot comparing apparent molecular weight calculated from the moments of the particle volume (eq 15) and from I_0 measurements (eq 14) assuming (filled triangles) no solvent entrapment and (open circles) solvent entrapment. The dashed line represents the parity line.

accounts for contributions from both asphaltene species and entrained solvent. Thus, the aggregate mass density and chemical composition values used in eq 13 to determine the aggregate scattering length density varied with the assumed amount of solvent entrapment. The mass densities of asphaltene solutions in toluene were measured using a 2 mL pycnometer. An average asphaltene dry mass density of 1.1 g/cm³ was calculated by extrapolating the solution data to pure solute. Mass densities of solvent mixtures and asphaltenes containing entrained solvent were calculated assuming no volume change upon mixing.

The z -averaged molecular weight of the aggregate, $\langle M_z \rangle$, is related to the zero- Q scattering intensity, I_0 , according to

$$\langle M_z \rangle = \frac{I_0 N_A d_m}{\phi(\Delta\rho)^2} \quad (14)$$

where N_A and d_m are Avogadro's number and the scatterer mass density, respectively. Alternatively, $\langle M_z \rangle$ is related to the first and second moments of the particle volume as given by

$$\langle M_z \rangle = \frac{N_A d_m \langle V^2 \rangle}{\langle V \rangle} \quad (15)$$

Equations 14 and 15 provide independent means of calculating the apparent aggregate z -averaged molecular weight from the fit parameters for the polydisperse oblate cylinder model. Because of difficulties in determining the average aggregate volume of a mass-fractal aggregate, it was not possible to determine the extent of solvent entrapment from the small particle mass-fractal and other nongeometric form factor models. Figure 8 compares the values of the apparent molecular weight obtained from these equations, assuming either that scatterers consist of dry asphaltenes with no entrained solvent (filled triangles) or assuming that the aggregates are solvated and therefore contain some amount of entrained solvent (open circles). With the assumption of no solvent entrapment, the average mass density (i.e., 1.1 g/cm³) and chemical composition of dry asphaltenes were used for the calculation of the solute-scattering length density. As shown in Figure 8, the values of the molecular weight obtained from eq 14 systematically overpredicted the values obtained from eq 15 by a factor of ~ 2.6 . This inconsistency in the calculated values suggests that asphaltenes are solvated to some extent by the solvent and that the entrained solvent contributes to the coherent

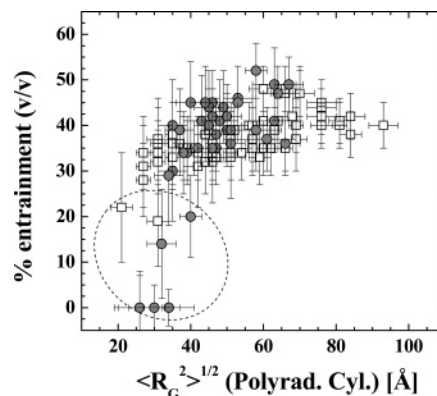


Figure 9. Variation in percentage of solvent entrapment with aggregate size for asphaltene fractions dispersed in (open squares) mixtures of *d*-heptane and *d*-toluene and (filled circles) mixtures of *d*-methyl naphthalene (or *d*-toluene) and *d*-methanol. Data points inside the dashed oval represent samples with a particle thickness less than 12 Å.

scattering of neutrons within the aggregates. The assumption of solvent entrapment affected the values of the solute mass density (d_m) and the mass fractions of the atomic species used in eq 13, thus reducing the scattering contrast between the solute and solvent. Similarly, changes in the solute mass density affected the values of the solute mass fraction (ϕ) used in eq 14. The amount of entrained solvent was determined for all samples individually by forcing the parity of eqs 14 and 15.

As shown in Figure 8, values of the aggregate molecular weight varied between 10 and 1000 kDa. Assuming a monomer mass of 1000 g/mol, this suggests that typical aggregates consisted of 10–1000 monomers. These aggregate molar masses may appear unreasonably high compared to values obtained from other methods, such as gel permeation chromatography or vapor pressure osmometry (VPO). For example, VPO of B6 and CS asphaltene fractions in toluene provided average aggregate molar masses between 2500 and 15 000 g/mol over a similar concentration range.²² However, it should be noted that SANS measures z -average molar masses, while VPO and other methods typically measure lower moments of the distribution. Therefore, molar masses obtained by SANS are more heavily weighted by a small percentage of very large aggregates. Aggregate molar masses corresponding to dimers, trimers, and small oligomers are not typically observed in the concentration regime of this study (i.e., 1% w/w), even from VPO. The largest molar masses observed that were on the order of 500–1000 kDa corresponded to either asphaltene subfractions that had lower overall solubility in the solvent mixtures because they were no longer stabilized by a more soluble asphaltene fraction or whole (i.e., unfractionated) asphaltenes in heptane-rich solvents. In both cases, small amounts of asphaltenes were flocculated (i.e., precipitated). The whole asphaltenes in toluene had average molar masses between 100 and 300 kDa from SANS.

Values of solvent entrapment within the aggregates are presented on a volume percent basis as a function of aggregate size, as shown in Figure 9. As indicated in the figure, a relatively narrow range of solvent entrapment values between ~ 20 and 50% (v/v) was observed for the asphaltenic fractions dispersed in mixtures of *d*-toluene and *d*-heptane. One sample (not shown in the figure) with a solvent entrapment value of 60% (v/v) represented the B6 P40 fraction dispersed in 70:30 *d*-toluene/*d*-heptane (v/v). Precipitation of significant amounts of asphaltenes was visually observed in this sample, suggesting an incorrect value of the scatterer volume fraction was used in the solvent entrapment calculation. Additional discussion concerning this

Table 4. Estimation of Solvent Entrainment for HO and GC Asphaltenes in Mixtures of Deuterated Toluene and Hydrogenated Toluene

asphaltene	vol % <i>d</i> -tol	I_0 (cm ⁻¹)	R_{avg} (Å)	L (Å)	σ_R (Å)	χ^2	$\langle R_G^2 \rangle^{1/2}$ (Å)	% ent
HO	100	2.11 ± 0.02	57.2 ± 0.9	24.3 ± 0.4	18.1 ± 0.2	3.7053	47 ± 5	47 ± 8
HO	80	1.27 ± 0.02	56 ± 1	18.7 ± 0.98	17.5 ± 0.3	1.7258	41 ± 6	40 ± 10
HO	60	0.65 ± 0.02	52 ± 3	26 ± 4	17.0 ± 0.2	0.9968	50 ± 7	50 ± 10
GC	100	1.90 ± 0.02	53.6 ± 0.8	24.2 ± 0.4	16.5 ± 0.2	4.1881	43 ± 5	43 ± 8
GC	80	1.09 ± 0.02	54 ± 2	26 ± 1	17.2 ± 0.5	1.4130	48 ± 7	50 ± 10
GC	60	0.59 ± 0.02	61 ± 6	18 ± 3	19 ± 2	0.7566	40 ± 10	40 ± 10

sample is presented in the next section. An apparent decrease in the extent of solvent entrainment was observed for the smallest aggregate formers (Figure 9). Data points inside the dashed oval represent samples with a particle thickness less than 12 Å and correspond to the same samples with larger than expected aspect ratios in Figure 6. It seems reasonable that, as the aggregate thickness approaches monomer dimensions, there is less internal volume inside the aggregates to allow solvent entrainment. Another observation is that the chemical composition of the asphaltene fractions more closely resembles that of petroleum resins, suggesting a possible difference in morphology between asphaltenes and resins. As previously stated, the polydisperse oblate cylinder model approximates the shape of asphaltenic aggregates. Therefore, perturbations from the oblate cylindrical shape are more significant at smaller aggregate sizes and are reflected by incorrect calculations of the particle volume that also affect the entrainment calculations. It is likely that the polydisperse oblate cylinder model inaccurately describes the scattering behavior of aggregates with particle thicknesses < 12 Å.

Additional evidence supporting the extent of solvent entrainment from asphaltene scattering curves is shown in Table 4. SANS experiments were performed on solutions of HO and GC asphaltenes (1% w/w) in mixtures of deuterated and hydrogenated toluene. These experiments allowed variation in the scattering length density of the solvent while maintaining the same solvating power for asphaltenes. As shown in the table, the experimental I_0 values decreased with increasing hydrogenation of the solvent; however, there were no significant changes in either the average size ($\langle R_G^2 \rangle$) or the shape (R , L , and σ_R) of the aggregates. There were also no significant changes in the amount of solvent entrainment in the aggregates, as calculated by the method described above, indicating that the analysis methods are internally consistent and further supporting the fact that solvent entrainment occurs in asphaltenic aggregates.

With regards to the molecular packing of asphaltenes within the aggregates determined from molecular recognition studies,^{28,32,69} the range of observed solvent entrainment values appears more consistent with the archipelago, rather than the continental-type, molecular structure. Aggregation of continental-type asphaltenes is dominated by stacking interactions of the aromatic regions, but is limited by steric interference from saturated rings and alkyl groups that are deformed out of plane with the aromatic moieties.²⁸ Solvent entrainment within the continental-type aggregates would likely be limited to the ~3.8 Å spacing between interacting aromatic moieties⁶⁹ and the saturated regions at the periphery of the aggregate where the enthalpy of adsorption for a solvent–asphaltene interaction is significantly lower.³² On the other hand, increased flexibility of aromatic and saturated hydrocarbon moieties in archipelago-type molecules enables the existence of grooves, channels, or internal cavities in the aggregate structure³² which would facilitate solvent entrainment to the extent observed in Figure 9.

The range of observed solvent entrainment values in Figure 9 is also consistent with similar values obtained from viscosity measurements performed on Ratawi vacuum residue asphaltenes in toluene,³⁹ Hassi Messaoud deposit asphaltenes in toluene,⁴⁰ and natural and synthetic Ratawi vacuum residue.⁴¹ In each of these studies, the degree of solvation ($S = \phi_{\text{m,dry}}/\phi_{\text{m,solvated}}$) was determined by application of Eilers equation to the relative viscosity (η_r) data. Eilers equation has the form

$$\frac{\eta_r^{1/2} - 1}{\phi} = \frac{[\eta]}{2} + \frac{\eta_r^{1/2} - 1}{\phi_m} \quad (16)$$

where $[\eta]$ and ϕ_m are the intrinsic viscosity and maximum particle packing fraction, respectively. The authors assumed a monodisperse hard-sphere geometry; therefore, ideal packing of a face-centered cubic was assumed for the “dry” asphaltene maximum packing fraction ($\phi_{\text{m,dry}} = 0.74$). Experimental values of $\phi_{\text{m,solvated}}$ were determined using eq 16. Typical values of the degree of solvation (S) ranged from 1.7 to 2.7 and corresponded to solvent entrainment values of 42–63% (v/v). The values obtained from viscosity measurements overlapped with the range of values observed from our SANS experiments, even though different assumptions were made concerning the aggregate geometries. Fenistein et al. approximated 97–98% (v/v) solvent entrainment from SANS measurements and 80–85% (v/v) entrainment from viscosity measurements performed on Safaniya vacuum residue asphaltenes ($\phi = 3$) in mixtures of *d*-heptane and *d*-toluene.⁴² The SANS and viscosity calculations were both performed assuming a monodisperse hard-sphere geometry for the aggregates. The lack of agreement between the calculated entrainment values from the SANS and viscosity methods suggests that the SANS method is more sensitive to the assumed aggregate geometry. A previous SANS study has shown that asphaltene aggregation is better described by a polydisperse oblate cylinder model than by a monodisperse sphere model.⁵³

The average aggregate molecular weight values presented in Figure 8 may be assumed to consist of a linear combination of molecular weight contributions from both dry asphaltene (M_{dry}) and entrained solvent components (M_{ent}), as given by

$$M_z = \phi_{\text{ent}} M_{\text{ent}} + (1 - \phi_{\text{ent}}) M_{\text{dry}} \quad (17)$$

where ϕ_{ent} is the volume fraction of entrained solvent within the aggregates. A direct comparison of the dry aggregate molecular weight values (M_{dry}) obtained from eqs 14 and 17 with and without the assumption of solvent entrainment is shown in Figure 10. As shown in the figure, different values of the apparent dry aggregate molecular weight were observed for the two assumptions. In fact, the value of M_{dry} for the assumption of solvent entrainment consistently overpredicted the corresponding value for the assumption of no solvent entrainment by a factor of ~1.6. The lack of parity between aggregate molecular weight values obtained from eqs 14 and 15 for the assumption of no solvent entrainment (Figure 8), as well as the lack of parity between dry aggregate molecular weight values (Figure 10), indicates that the inclusion

(69) Murgich, J.; Rodriguez, J.; Aray, Y. *Energy Fuels* **1996**, *10* (1), 68–76.

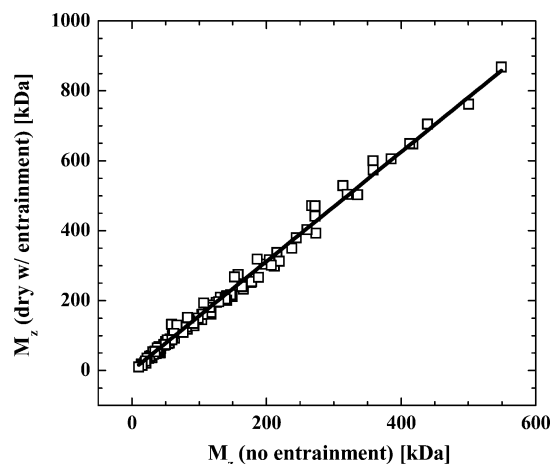


Figure 10. Average aggregate molecular weight (dry) for the assumption of solvent entrapment compared to the average aggregate molecular weight for the assumption of no solvent entrapment. Solid line represents the best-fit line through the data.

of solvation effects is essential for the accurate calculation of the average aggregate molecular weight.

Asphaltene Flocculation. Using the calculated solvent entrapment values, attempts were made to estimate the relative amounts of asphaltenic material present in micron-scale flocs versus nanoparticle aggregates. Since the spread of solvent entrapment values for asphaltenes in mixtures of *d*-toluene and *d*-heptane (Figure 9) was relatively narrow for aggregates dispersed in mixtures of *d*-toluene and *d*-heptane, an average solvent entrapment value of 40% (v/v) was assumed for all samples with $R_G > 50 \text{ \AA}$. The total volume fraction of scatterers (ϕ_{total}) was calculated based on this assumed value of solvent entrapment. As previously discussed, the effective contribution of microparticle scatterers was modeled as a power-law function and subtracted from the composite scattering curves for those spectra containing significant low- Q upturns. Thus, the polydisperse cylinder fits applied to power-law-corrected scattering curves revealed information concerning the scattering behavior of nanoparticles only. The volume fraction of nanoparticle scatterers (ϕ_{nano}) was calculated from eq 12, using the I_0 , $\langle V \rangle$, and $\langle V^2 \rangle$ parameters obtained from the polydisperse cylinder fits and the scattering contrast calculated for the assumption of 40% (v/v) solvent entrapment. The volume fraction of microparticle scatterers (ϕ_{flocs}) was thus given by

$$\phi_{\text{flocs}} = \frac{\phi_{\text{total}} - \phi_{\text{nano}}}{\phi_{\text{total}}} \quad (18)$$

A comparison of individual microparticle volume fractions obtained from SANS experiments to volume fractions of precipitated material observed from gravimetric experiments²² is presented in Table 5. As indicated in the table, the volume fraction of precipitated material observed from the gravimetric experiments was generally less than 0.06 for the samples shown with a few exceptions. Unfortunately, the accuracy of the microparticle volume fraction from the SANS experiments was poor, particularly for asphaltene samples in the soluble solvent regime, as uncertainty in the results was propagated from the power-law corrections, polydisperse cylinder model fitting, and subsequent solvent entrapment calculations. The SANS microparticle volume fractions presented in Table 5 provided estimates that roughly trended with the gravimetric results. One interesting observation was that the amount of flocculated material

Table 5. Volume Fraction of Microparticles from SANS for Various Asphaltene Fractions in Mixtures of *d*-Heptane (H) and *d*-Toluene (T) in Comparison to the Precipitated Volume Fraction from Gravimetric Experiments

solute		solvent		SANS		gravimetric
asphaltene	fraction	vol % T	vol % H	$\langle R_G^2 \rangle^{1/2}$ (Å)	ϕ_{flocs}	ϕ_{ppt}
AH	P30	100	0	58 ± 3	0.00	0.01
AH	P30	50	50	60 ± 3	0.00	0.02
B6	Whole	100	0	62 ± 4	0.00	0.00
B6	Whole	60	40	72 ± 3	0.00	0.02
B6	Whole	55	45	72 ± 3	0.00	0.01
B6	P40	100	0	131 ± 5	0.05	0.05
B6	P40	90	10	118 ± 5	0.09	0.03
B6	P40	80	20	107 ± 5	0.19	0.06
B6	P40	70	30	73 ± 9	0.57	0.36
CS	Whole	100	0	63 ± 3	0.01	0.00
CS	Whole	80	20	79 ± 7	0.03	0.01
CS	Whole	70	30	78 ± 3	0.04	0.01
CS	Whole	60	40	90 ± 4	0.06	0.01
CS	Whole	55	45	113 ± 5	0.06	0.02
CS	Whole	45	55	92 ± 5	0.26	0.27
CS	P40	100	0	98 ± 5	0.25	0.00
CS	P40	90	10	106 ± 6	0.17	0.01
CS	P40	80	20	97 ± 6	0.24	0.03
CS	P40	50	50	84 ± 5	0.28	>0.51
HO	Whole	100	0	51 ± 3	0.00	0.00
HO	Whole	60	40	73 ± 2	0.01	0.01
HO	P39	100	0	107 ± 4	0.03	0.00
HO	P39	90	10	118 ± 5	0.00	0.01
HO	P39	80	20	106 ± 5	0.09	0.01

from the SANS measurements generally increased with increasing amounts of heptane flocculant. Furthermore, the largest amounts of flocculated material were observed for the three samples in the insoluble solvent regime (i.e., B6 P40 in 60% toluene, CS whole in 45% toluene, and CS P40 in 50% toluene). For the case of CS whole asphaltenes in 45% toluene, the amount of precipitated/flocculated material from the two measurement methods agreed within 5%. More accurate estimates of microparticle flocculation would likely be obtained by probing larger length scales of aggregation by ultra-SANS (USANS) (or ultra-SAXS (USAXS)) measurements.

Conclusions

Small-angle scattering measurements were performed on 108 solutions of asphaltenes dispersed in deuterated solvents. The measured samples possessed wide diversity in the chemical composition of the asphaltenes (e.g., H/C from 1.09 to 1.45 and heteroatom contents of 2.5–6 wt %), as well as variation in the quality of the solvent for dispersing asphaltenes. In many cases, aggregates of HO and B6 asphaltenes were further dispersed with the addition of *d*-methanol. Scattering intensity curves were fit to the Guinier approximation, the Ornstein–Zernike (or Zimm) model, a mass-fractal model, and a polydisperse cylinder model. Comparison of the fitting parameters obtained from the various models indicated that the values of I_0 and R_G obtained for a given sample are highly model-dependent. Similarly, values of the apparent aggregate fractal dimension appeared to vary depending on the method of analysis. For example, the molecular weight versus aggregate size scaling relationship from the Ornstein–Zernike analyses provides a value of the apparent fractal dimension ($D \sim 2$) that was independent of solute and solvent composition. However, values of the apparent fractal dimension from the mass-fractal fits appeared to decrease with increasing aggregate size, suggesting that the smallest aggregate formers

were more globular with little surface roughness (i.e., $D \sim 3$), while the largest aggregate formers were more dendritic with higher surface roughness ($D \sim 2.2\text{--}2.4$). Inconsistencies in the I_0 , R_G , and D parameters between the Ornstein–Zernike and mass-fractal models suggest that the molecular structures of asphaltene aggregates are probably not consistent with that of a mass fractal.

Geometry-dependent form factor models, such as the polydisperse cylinder model, provide additional volume information that allows accurate calculation of the aggregate molecular weight and extent of solvent entrainment. The polydisperse oblate cylinder model used in this study provided agreement with the Guinier parameters, although this agreement appeared to diminish with increasing aggregate size. Typical values of the aggregate thickness from the polydisperse cylinder fits ranged from 5 to 32 Å, while the average particle radius ranged from 25 to 125 Å. The polydispersity in the particle radius appeared to be independent of the particle size ($\sim 30\%$). Assuming that an asphaltene monomer consists of groups of condensed aromatic rings containing polar moieties that are interconnected by aliphatic chains, the asphaltene aggregation mechanism might proceed through a series of localized stacking interactions of aromatic rings. The physical linkage of one ring system to another in a monomer somewhat increases the particle thickness, but significantly expands the aggregate in the radial dimension, where polydispersity in the aggregate size is most evident.

Discrepancies between average aggregate molecular weight values obtained from two independent methods suggested the need to include the solvation effects in the calculations. Solvent entrainment within the aggregates roughly varied from 30 to 50% (v/v) and was consistent with solvation values obtained from viscosity measurements found in the literature. Lower estimates of the percent solvent entrainment were observed as the particle thickness approached the monomer dimensions and

were attributed to a decrease in the internal volume available for solvent entrainment.

Attempts to use the observed solvent entrainment values to estimate the relative proportions of microscale and nanoscale aggregates in solution were limited in accuracy; however, the volume fraction of microscale flocs generally increased with decreasing solvent quality. Furthermore, flocculation was only observed to be greater than 20% for those samples that were dispersed in an insoluble solvent regime. Beyond the calculation of aggregate sizes, the inclusion of solvent entrainment is crucial for the calculation of additional parameters from the scattering data, including the aggregate molecular weight and the estimation of flocculated material.

Acknowledgment. This research is supported by the Petroleum Environmental Research Forum, ExxonMobil, Shell, Equilon, ChevronTexaco, Nalco Energy Services Division, Champion Technologies, National Science Foundation Grants (CTS981727), and the NSF Graduate Research Fellowship Program. We acknowledge Darlene Mahlow at the University of Alberta for performing combustion elemental analyses on the asphaltene and resin samples. This work benefited from the use of facilities in the Intense Pulsed Neutron Source and the Chemistry Division, which is funded by the U. S. Department of Energy, Office of Basic Energy Sciences under contract W-31-109-ENG-38 to the University of Chicago. We would particularly like to thank Pappannan Thiyagarajan and Denis Wozniak of the Intense Pulsed Neutron Source Division at Argonne National Laboratory for their assistance with the SAND instrument. We would also like to thank Matthew B. Smith, M. Lupe Marques, and Vincent Verruto for helping with the sample preparation and SANS data collection.

LA052509J